



Cite this: *Chem. Commun.*, 2024, 60, 2208

Received 20th December 2023,
Accepted 17th January 2024

DOI: 10.1039/d3cc06189b

rsc.li/chemcomm

An NIR-emitting cyanine dye with pyridinium groups: the impact of regio-bond connection on the photophysical properties†

Yonghao Li,^a Matthew A. Tuttle,^b Qin Liu^b and Yi Pang^{id} ^{*,a}

Two ESIPT-based isomeric cyanines were synthesized with significant bathochromic shift in the optical absorption λ_{abs} and emission λ_{em} , along with a very large Stokes shift. Probe 2 exhibited a longer conjugation and better photostability. Both compounds exhibited good selectivity for labeling the plasma membrane of prokaryotic cells and the hair cells of zebrafish.

Hearing disorders or deafness are common diseases that can be age-related, or noise- or certain ototoxic drug-induced.^{1,2} In the U.S., about 1 in every 8 individuals in the working population have hearing difficulty.³ Most hearing loss is related to the irreversible damage of sensory hair cells in the inner ear,^{4,5} which is often induced by exposure to loud noises⁶ or certain chemicals/drugs that can kill the hair cells in the inner ear. Management of hearing loss requires identification of methods that can stimulate hair cell regeneration in mammals. Due to the limited ability for mammals to regenerate sensory hair cells,⁷ there is significant interest in studying the sensory hair cells of non-mammalian vertebrates such as zebrafish, whose hair cells can be readily regenerated after damage.^{8–14} Recently, zebrafish have been recognized as an excellent animal model to study hair cell development and regeneration, as the zebrafish lateral line opens the gate to identifying the complex signaling events triggered by injury and regeneration.^{4,5,7,15–17}

Zebrafish lateral line hair cells are located in the center of a mechanosensory organ known as the neuromast, where the hair cells are surrounded by inner support cells and an outer ring of mantle cells^{4,5,18} (Fig. 1). Neuromasts can be marked by specific fluorescent dyes such as 4-Di-2-ASP.^{19–21} Development of improved imaging methods is desirable to aid these studies.

Excited state intramolecular proton transfer (ESIPT) has emerged to be a powerful strategy in designing fluorescent

molecular probes, as they often exhibit unusually large Stokes shifts ($\Delta\lambda \geq 150$ nm) and dual emission for ratiometric sensing. However, the majority of known ESIPT-based sensors give green-red emission, with very few giving near-infrared emission (NIR-I, 650–950 nm) that is desirable for imaging applications (especially for *in vivo*). Despite recent progress, it remains a challenge to tune the emission of this class of materials to well above 700 nm. In an effort to search for new dyes with improved optical characteristics, we recently reported that probe 1 with a pyridinium terminal group can label neuromast hair cells on wild type zebrafish.^{22,23} Due to the presence of excited state intramolecular proton transfer (ESIPT), probe 1 exhibits a large Stokes shift ($\Delta\lambda \sim 260$ nm) and a good quantum yield. In comparison with the styryl dye 4-Di-2-ASP ($\lambda_{em} \approx 590$ –610 nm, depending on the solvents), the emission of probe 1 occurs at a longer wavelength ($\lambda_{em} \approx 684$ nm in CH_2Cl_2).^{22,23} We now report an improved version by synthesis of 2 and 3 that includes a furan group in the styryl pyridinium segment for extended π -conjugation (Scheme 1). Inclusion of the furan group effectively tunes the emission towards an even longer wavelength (to well above 700 nm) while retaining their cellular selectivity, making them even more attractive for imaging applications (e.g. neuromast labeling and staining of *E. coli* membranes).

Synthesis. Compounds 2 and 3 were synthesized *via* Suzuki coupling reaction in good yields. The products were characterized

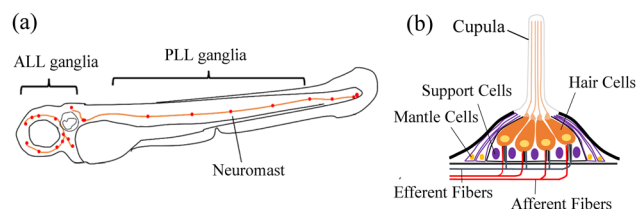


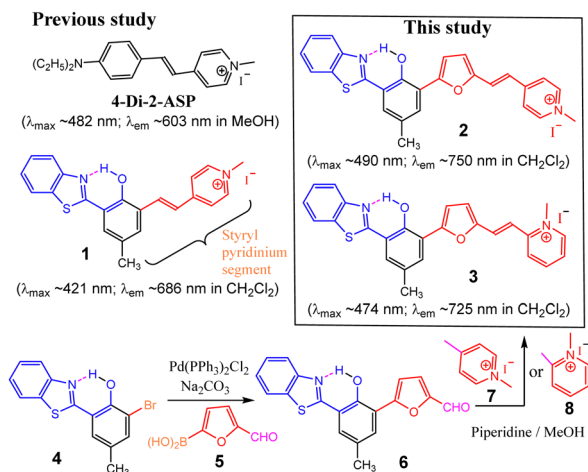
Fig. 1 Zebrafish lateral line neuromasts. (a) Schematic depicting a larval zebrafish. Red patches indicate the location of neuromasts in the lateral line (LL) system. Orange patches represent the location of the anterior (ALL) and posterior (PLL) LL ganglia. (b) A side view of a single LL neuromast structure.

^a Department of Chemistry, University of Akron, Akron, Ohio 44325, USA.
E-mail: yp5@uakron.edu

^b Department of Biology, University of Akron, Akron, Ohio 44325, USA

† Electronic supplementary information (ESI) available. See DOI: <https://doi.org/10.1039/d3cc06189b>





Scheme 1 The structures of commercial styryl dye and ESIPT compounds, along with their absorption and fluorescence.

by ¹H-NMR and ¹³C-NMR spectroscopy, and ESI-MS (see ESI,† Fig. S1–S9 for details).

Photophysical properties. In comparison with the styryl dye (4-Di-2-ASP) that has a small Stokes shift (Δλ ~ 21 nm in CH₂Cl₂), the ESIPT dyes (**1–3**) revealed a quite large Stokes shift (Δλ > 250 nm in CH₂Cl₂) (Table 1).^{22–24} As a consequence of including the furan ring in the structure, the absorption and emission of **2** (λ_{max} ~ 490 nm, λ_{em} ~ 750 nm in CH₂Cl₂) exhibited a significant bathochromic shift (by ~ 70 nm) from **1** (λ_{max} ~ 421 nm, λ_{em} ~ 686 nm in CH₂Cl₂). Interestingly, both **2** and **3** maintained reasonably high fluorescence (e.g. φ_f ~ 0.26 for **1** in CH₂Cl₂), which makes them suitable for imaging. In addition, the fluorescence quantum yield of **2** decreased dramatically in an aqueous medium (e.g., φ_f ~ 0.003 for **2**), showing a large solvent effect (ESI,† Fig. S10–S13). Drastic fluorescence quenching in H₂O would be useful for minimizing fluorescence background.

Interestingly, compounds **2** and **3** exhibit a minor fluorescence peak at 570–590 nm, especially in CH₂Cl₂ (Fig. 2), which is not present in compound **1**.^{22,24} In addition, the relative intensity of the minor peak has no significant change over a wide concentration range (2–10 μM) (ESI,† Fig. S14 and S15). This minor

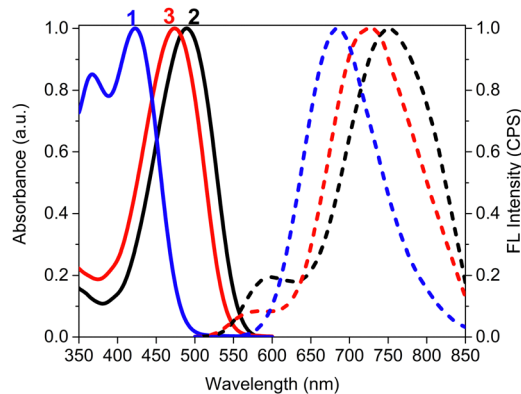


Fig. 2 UV-vis absorption (dotted line) and fluorescence spectra (solid line) of fluorescent dyes **2** (black), **3** (red) and **1** (blue) in DCM with a large Stokes shift.

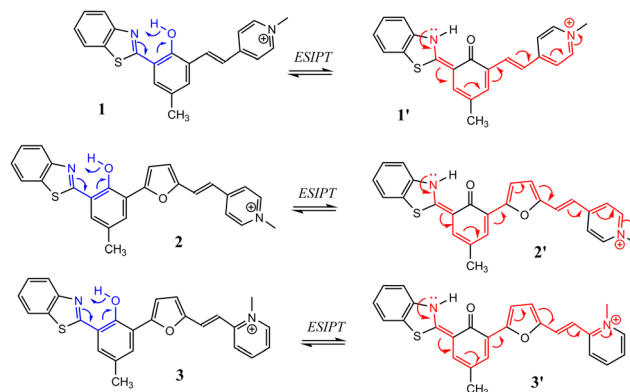
fluorescence peak was not associated with H-aggregation, as its content was not increased in less concentrated solution.

In order to understand the origin of the observed minor fluorescence peaks, time-dependent density functional theory (TD-DFT) was used to calculate their UV-Vis and fluorescence spectra in CH₂Cl₂ (ESI,† Fig. S16–S19). The calculated absorption peaks from the enol forms of **2** and **3** were at 490 nm and 474 nm (ESI,† Fig. S16 and S18), respectively, which matched well with their experimental values (λ_{abs} = 490 nm and 483 nm). The calculation also showed that the fluorescence of the enol forms of **2** and **3** were at 588 and 583 nm, respectively. The results thus pointed to the fact that the minor emission peaks observed at 570–590 nm (Fig. 2) could be attributed to the enol tautomer. The major emission peaks at ~700 nm could be attributed to the keto form, in agreement with the ESIPT mechanism.^{23,25} The fluorescence spectra (Fig. 2) thus suggested that ESIPT remained to be a predominant process for new probes **2** and **3**, giving major emission from their keto tautomer while having minor emission from the enol forms.

It should be noticed that the emission wavelength is dependent on the extent of intramolecular charge transfer (ICT) in their respective keto tautomer, which is enabled by ESIPT (Scheme 2).^{23,24} Thus, the emission of **2** would occur at a longer

Table 1 Photophysical properties of compounds **1–3** in different solvents

		DCM	DMSO	MeOH	H ₂ O	MeCN
1	λ _{abs} /nm	421	395	401	392	397
	ε/M ⁻¹ cm ⁻¹	28 133	35 249	32 984	29 683	26 103
	λ _{em} /nm	686	701	695	697	690
	φ _f	0.34	0.25	0.18	0.06	0.19
2	λ _{abs} /nm	490	447	457	450	448
	ε/M ⁻¹ cm ⁻¹	42 957	39 128	65 417	15 410	41 851
	λ _{em} /nm	750	790	770	770	770
	φ _f	0.266	0.115	0.109	0.003	0.115
3	λ _{abs} /nm	474	437	445	440	436
	ε/M ⁻¹ cm ⁻¹	35 445	36 679	41 811	25 075	38 521
	λ _{em} /nm	725	759	743	770	738
	φ _f	0.183	0.180	0.165	0.009	0.172



Scheme 2 Schematic illustration of the formation of the keto form via excited state intramolecular proton transfer (ESIPT). And the intra-molecular charge transfer.



wavelength than that of its isomer **3**, as the keto tautomer of the former (**2'**) had a more extended ICT interaction (involving two C=C bonds in the pyridinium ring, Scheme 2). This was further supported by a computational study, which revealed that **2** had a lower HOMO–LUMO energy gap than **3** (ESI,† Fig. S20), consistent with the experimental observation.

Compounds **2** and **3** generated a new peak at 550–580 nm and became non-fluorescent in the NIR range when pH > 7 (ESI,† Fig. S21–S25), as the deprotonation occurred to give aromatic anion Ar–OH → Ar–O[−]. With Boltzmann's fitting, the pK_a values of **2** and **3** were determined to be similar at 6.6 and 6.5, respectively (ESI,† Fig. S23 and S26), which is notably different from that of **1** (pK_a = 8.26). The phenolic proton in **2** and **3** becomes more acidic, induced by the furan group, which is in good agreement with the observed ¹H NMR (δ = 13.31 ppm for the phenolic proton in DMSO).

In order to evaluate the photostability, the solution of **2** and **3** in CH₂Cl₂ was irradiated with a blue LED light (455–465 nm, 7000–8000 mcd), while the absorption spectrum was monitored at different time intervals. Interestingly, compound **2** exhibited significantly better stability than its isomer **3** (Fig. 3), under the same conditions. This result showed a large impact of *regio*-bond connection (ESI,† Fig. S27 and S28).

The response of **2** and **3** to anionic and cationic species was also examined. Common metal cations such as Na⁺, K⁺, Co³⁺, Al³⁺, Ag⁺, Hg⁺, Pd²⁺, Zn²⁺, Mg²⁺, and Ni²⁺ exhibited basically no interference in both absorption and emission (ESI,† Fig. S29, S30, S33, S34). Biologically important anions, such as ATP, ADP, AMP, Br[−], I[−], HPO₄^{2−} and citrate, were found not to interfere with the emission of probe **2**. Although basic anions (*e.g.* PO₄^{3−}, CO₃^{2−} and acetate (OAc[−])) were found to cause a significant change in absorption and fluorescence spectra (ESI,† Fig. S31 and S32), due to deprotonation of phenol, and they would have little impact on the potential imaging applications due to their low abundance in biological systems.

Bioimaging study. The presence of similar terminal groups as **1** encouraged us to examine new probes **2** and **3** for potential labeling of the *E. coli* cell membrane and hair cells on zebrafish (see ESI† for details, All animal related procedures were

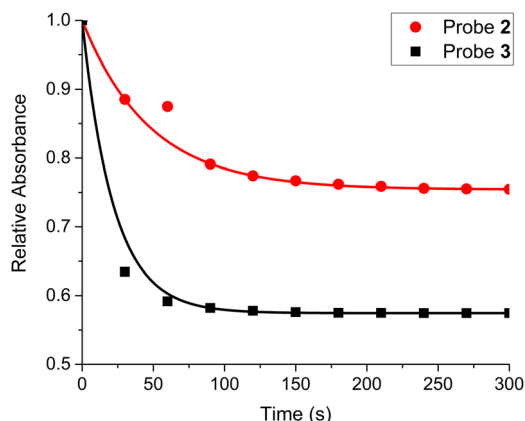


Fig. 3 Comparison of photostability for **2** and **3** in DCM (10 μM), by monitoring the decay of λ_{abs}.

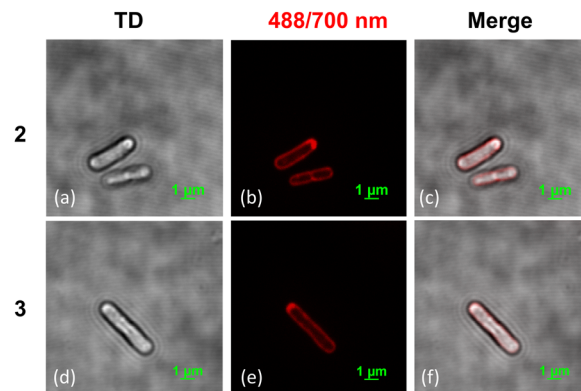


Fig. 4 Fluorescent confocal microscope images of *E. coli* cells stained with 1 μM compound **2** (a)–(c) and **3** (d)–(f) in TD (a) and (d), excitation/emission = 488/700 nm (b) and (e) and overlap (c) and (f) under magnification of 100× and digitally enhanced by 10 times.

approved by the Institutional Animal Care and Use Committee at The University of Akron (D16-00501)).^{22,24} Thus, these new probes were used to stain *E. coli* cells. Clear fluorescence signals could be observed with low concentration of dye (1 μM) (Fig. 4(b) and (e)), showing that both probes exhibited good selectivity to stain the plasma membrane (Fig. 4(c) and (f)). In order to compare their relative stability, the stained *E. coli* cells (with 1 μM of **2** and **3**) were continuously irradiated for two minutes (ESI,† Fig. S37). Interestingly, the cells stained with **2** retained 77% average fluorescence intensity, while those stained with **3** only have 56% intensity remaining. The observation indicated that **2** had better photostability than **3**, which was consistently observed in CH₂Cl₂ (Fig. 3) and in H₂O (ESI,† Fig. S39).

Compounds **2** and **3** were further used to investigate their potential imaging applications in zebrafish. When the probes were used to stain zebrafish embryos, nonuniform fluorescence signals were observed on the fish's body, indicating selective labeling (Fig. 5 and ESI,† Fig. S38). The labeling pattern by using **2** or **3** was comparable to that using 4-Di-2-ASP (Fig. 5(a)–(d) and ESI,† Fig. S38(a), (d)), showing selective labeling of neuromasts. Although the new probes were used in a lower concentration (10 μM) in comparison with 4-Di-2-ASP (50 μM), they gave comparable fluorescence intensity during the imaging study (Fig. 5 and ESI,† Fig. S38).²⁶ Both probes labeled the central region of the neuromasts where hair cells are located. In summary, both **2** and **3** labeling were nearly identical with the commercial dye 4-Di-2-ASP (Fig. 5(d)–(f)). Probes **2** and **3** would be an attractive alternative to the commercial 4-Di-2-ASP for hair cell labeling, due to their attractive photophysical properties (*e.g.* large Stokes shift and NIR emission).

Two NIR-emitting (> 700 nm) ESIPT dyes **2** and **3** were synthesized in high yield, to examine the impact of a furan group in the styryl pyridinium segment. Inclusion of a furan ring in the styryl segment is found to extend π-conjugation effectively, while retaining the desired cellular selectivity for zebrafish neuromasts and *E. coli* membrane. The attractive optical properties of **2** (λ_{abs} ≈ 490 nm, λ_{em} ≈ 770 nm) make it a rare example of a NIR-emitting fluorophore that exhibits



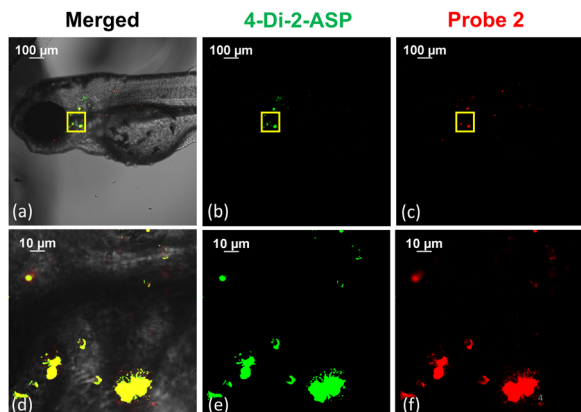


Fig. 5 Confocal images of zebrafish embryos (72 hpf) labeled with 4-Di-2-ASP (b) and (e) and probe 2 (c) and (f), merged (a) and (d) under 10× (first row) and 100× (second row) magnification. Excitation/emission = 488/595 nm for 4-Di-2-ASP, and excitation/emission = 488/700 nm for probe 2.

very large Stokes shift and high fluorescence ($\phi_{\text{fl}} \approx 0.26$ in CH_2Cl_2). Optical comparison between 2 and 3 reveals a moderate difference in the absorption and emission wavelengths, attributed to the impact of *regio*-bond connection on the pyridinium ring. This finding is further supported by the TD-DFT calculation.

Molecular imaging studies show that both probes 2 and 3 are useful for labeling the plasma membrane of prokaryotic cells and hair cells of zebrafish with good selectivity, although the former is found to be more photolytically stable. The study thus successfully demonstrates that new probe 2 could be an attractive candidate for imaging hair cells, due to its good cellular selectivity, NIR emission ($\lambda_{\text{em}} \approx 770$ nm) with large Stokes shift, and improved photostability. Such an imaging tool could play an important role to aid the study of the regeneration of hair cells and screening/evaluation of *ototoxic* drugs.

Conceptualization, Y. P., methodology, Y. P., Y. L., formal analysis, Y. L. and Y. P., investigation, Y. L. and M. T., resources, Y. L. M. T. and Q. L., data curation, Y. L. Q. L. and Y. P., writing – original draft preparation, Y. L., writing – review and editing, Q. L. and Y. P., supervision, Y. P., funding acquisition, Y. P. All authors have read and agreed to the published version of the manuscript.

This research was financed by NIH (Grant no. 1R15GM126438-01A1). Y. P. also acknowledges partial support from Coleman Endowment from The University of Akron.

Conflicts of interest

There are no conflicts to declare.

Notes and references

- N. Oishi and J. Schacht, *Expert Opin. Emerging Drugs*, 2011, **16**, 235–245.
- J. G. Yorgason, J. N. Fayad and F. Kalinec, *Expert Opin. Drug Saf.*, 2006, **5**, 383–399.
- E. Kerns, E. A. Masterson, C. L. Themann and G. M. Calvert, *Am. J. Ind. Med.*, 2018, **61**, 477–491.
- M. E. Lush and T. Piotrowski, *Dev. Dyn.*, 2014, **243**, 1187–1202.
- L. Jiang, A. Romero-Carvajal, J. S. Haug, C. W. Seidel and T. Piotrowski, *Proc. Natl. Acad. Sci. U. S. A.*, 2014, **111**, E1383–E1392.
- S. W. Tak, R. R. Davis and G. M. Calvert, *Am. J. Ind. Med.*, 2009, **52**, 358–371.
- E. W. Rubel, S. A. Furrer and J. S. Stone, *Hear. Res.*, 2013, **297**, 42–51.
- M. E. Warchol, *Hear. Res.*, 2011, **273**, 72–79.
- B. C. Cox, R. Chai, A. Lenoir, Z. Liu, L. L. Zhang, D. H. Nguyen, K. Chalasani, K. A. Steigelman, J. Fang, A. G. Cheng and J. Zuo, *Development*, 2014, **141**, 816–829.
- J. C. Burns, B. C. Cox, B. R. Thiede, J. Zuo and J. T. Corwin, *J. Neurosci.*, 2012, **32**, 6570–6577.
- J. C. Burns and J. T. Corwin, *Hear. Res.*, 2013, **297**, 52–67.
- O. Bermingham-McDonogh and E. W. Rubel, *Curr. Opin. Neurobiol.*, 2003, **13**, 119–126.
- H. López-Schier and A. J. Hudspeth, *Proc. Natl. Acad. Sci. U. S. A.*, 2006, **103**, 18615–18620.
- E. Y. Ma, E. W. Rubel and D. W. Raible, *J. Neurosci.*, 2008, **28**, 2261–2273.
- J. Liang, D. Wang, G. Renaud, T. G. Wolfsberg, A. F. Wilson and S. M. Burgess, *J. Neurosci.*, 2012, **32**, 10662–10673.
- H. R. Brignull, D. W. Raible and J. S. Stone, *Brain Res.*, 2009, **1277**, 12–23.
- K. N. Owens, D. E. Cunningham, G. Macdonald, E. W. Rubel, D. W. Raible and R. Pujol, *J. Comp. Neurol.*, 2007, **502**, 522–543.
- E. Y. Ma and D. W. Raible, *Curr. Biol.*, 2009, **19**, R381–R386.
- S. W. Chou, Z. Chen, S. Zhu, R. W. Davis, J. Hu, L. Liu, C. A. Fernando, K. Kindig, W. C. Brown, R. Stepanyan and B. M. McDermott, *Nat. Commun.*, 2017, **8**, 1–16.
- P. P. Hernández, V. Moreno, F. A. Olivari and M. L. Allende, *Hear. Res.*, 2006, **213**, 1–10.
- A. B. Coffin, H. Brignull, D. W. Raible and E. W. Rubel, *In The Lateral Line System*, S. Coombs, H. Bleckmann, R. R. Fay, A. N. Popper, Eds., Springer New York, NY, 2014, pp. 313–347.
- L. McDonald, D. Dahal, M. Konopka, Q. Liu and Y. Pang, *Bioorg. Chem.*, 2019, **89**, 103040.
- Y. Li, D. Dahal, C. S. Abeywickrama and Y. Pang, *ACS Omega*, 2021, **6**, 6547–6553.
- D. Dahal, K. R. Ojha, N. Alexander, M. Konopka and Y. Pang, *Sens. Actuators, B*, 2018, **259**, 44–49.
- A. C. Sedgwick, L. Wu, H.-H. Han, S. D. Bull, X.-P. He, T. D. James, J. L. Sessler, B. Z. Tang, H. Tian and J. Yoon, *Chem. Soc. Rev.*, 2018, **47**, 8842–8880.
- L. Magrassi, D. Purves and J. W. Lichtman, *J. Neurosci.*, 1987, **7**, 1207–1214.

